PHILOSOPHICAL TRANSACTIONS A

rsta.royalsocietypublishing.org

Research

Cite this article: Kun F, Pál G, Varga I, Main IG. 2018 Effect of disorder on the spatial structure of damage in slowly compressed porous rocks. *Phil. Trans. R. Soc. A* **377**: 20170393.
http://dx.doi.org/10.1098/rsta.2017.0393

Accepted: 16 August 2018

One contribution of 15 to a theme issue 'Statistical physics of fracture and earthquakes'.

Subject Areas:
computational physics, geophysics, complexity, statistical physics, mechanics

Keywords:
damage band, fault, compression, fragmentation, disorder, discrete element simulation

Author for correspondence:
F. Kun
e-mail: ferenc.kun@science.unideb.hu

Effect of disorder on the spatial structure of damage in slowly compressed porous rocks

Ferenc Kun[1], Gergő Pál[2], Imre Varga[3] and Ian G. Main[4]

[1]Department of Theoretical Physics, University of Debrecen, PO Box 5, 4010 Debrecen, Hungary
[2]Institute for Nuclear Research, Hungarian Academy of Sciences (Atomki), PO Box 51, 4001 Debrecen, Hungary
[3]Department of Informatics Systems and Networks, University of Debrecen, PO Box 12, 4010 Debrecen, Hungary
[4]School of Geosciences, University of Edinburgh, Edinburgh EH9 3FE, UK

FK, 0000-0001-6469-7917

Faults and damage zone properties control a range of important phenomena, from the hydraulic properties of underground reservoirs to the physics of earthquakes on a larger scale. Here, we investigate the effect of disorder of porous rocks on the spatial structure of damage emerging under compression. Model rock samples are numerically generated by sedimenting particles where the amount of disorder is controlled by the particle size distribution. To obtain damage bands with a sufficiently large length along axis, we performed simulations of 'Brazilian'-type compression tests of cylindrical samples. As failure is approached, damage localization leads to the formation of two conjugate shear bands. The orientation angle of bands to the loading direction increases with disorder, implying a decrease in the internal coefficient of friction. The width of the damage band scales as a power law of the degree of disorder. Inside the damage band, the sample is crushed into a large number of pieces with a power law mass distribution. The shape of fragments undergoes a crossover at a disorder-dependent size from the isotropy of small pieces to the anisotropic flattened form of the large ones. The results provide important constraints in understanding the role of disorder in geological fractures.

This article is part of the theme issue 'Statistical physics of fracture and earthquakes'.

THE ROYAL SOCIETY PUBLISHING

1. Motivations

Compressive failure of brittle heterogeneous materials is accompanied by the spontaneous formation of localized damage bands, where the final slip occurs at global failure. On larger length scales, natural faults often contain fragmented rocks created by fracturing, crushing and milling during the relative motion of the two rock bodies along the fault [1–4]. Understanding the properties of damage zones is important because a broad range of phenomena—including the hydraulic properties of underground reservoirs, the frictional conditions and stability of faults, and the emergence of natural catastrophes such as landslides and earthquakes—strongly depend on their internal structure and relationship to the host rock [1,5].

The amount of inherent structural disorder present at the meso- and micro-scale of materials plays a crucial role in the emergence of damage bands and their properties, including also their final position, orientation and internal structure. With some notable exceptions, it is a difficult challenge to construct synthetic materials with controlled disorder for laboratory experiments. For example, subcritical crack propagation was investigated in a sheet of paper under a constant external load, where the paper was softened by introducing holes in different geometries. It was found that the increasing disorder slows down the propagation of the crack [6]. More recently, experimental and theoretical studies have revealed that the amount of structural disorder of materials has a substantial effect on the time evolution of damage. Specifically, increasing disorder results in a more intense avalanche activity, improving the prediction of the time of ultimate failure [7]. These studies confirm that the degree of controlled disorder strongly controls the time evolution of damage in the approach to catastrophic failure.

In our present study, we focus on the effect of the amount of disorder on the spatial structure of damage using a discrete element model (DEM) of porous rocks. To build numerical rock samples, we simulate the sedimentation process of spherical particles in a cylindrical container. We use a realistic lognormal distribution of the particle radius where the degree of disorder could be varied by tuning the parameters of the distribution (equivalent to the geometric mean and geometric standard deviation). To form a sedimentary rock sample, the particles are connected by beam elements which represent the cementation between grains. Our model construction has the advantage that the random homogeneous packing of particles is the only source of disorder which determines the physical properties of cohesive elements.

Laboratory testing of porous rocks is dominated by uniaxial test geometries where cylindrical samples are subject to strain- or stress-controlled loading [8–10]. Here, we use one of the other major standards of rock mechanics—the 'Brazilian' test—with a modified geometrical set-up and boundary conditions [11]. In the Brazilian or indirect tensile test, a disc, with a typical height-to-diameter ratio of 0.5–0.6, is loaded in a diametral plane by point forces applied at opposite ends of a diameter [11]. In our study, simulations are also performed with cylindrical samples which are loaded diametrically. However, in order to promote shear failure and the formation of damage bands, the load is applied on a longer cylinder over an extended surface area of the sample which is clamped. This type of modified Brazilian set-up has the advantage that the geometrical constraints and the translational symmetry of the system along the longer cylinder axis give rise to the emergence of extended damage bands in a well-controlled way. Here, we demonstrate that under such conditions a set of conjugate deformation bands emerges spontaneously to accommodate the boundary strain, and that the properties of the band and its internal structure depend strongly on the degree of disorder in the original model rock.

2. Porous rock with controlled disorder

In order to construct rock samples on the computer with controlled porous microstructure, we simulated the sedimentation process of particles inside a cylindrical container. Spherical particles were sedimented under the action of gravity and lost their kinetic energy by colliding with the particles of the growing sediment layer and with the container wall. The height H to diameter D ratio $h = H/D$ of the cylinder was fixed to $h = 2.3$ according to the typical geometrical layout of

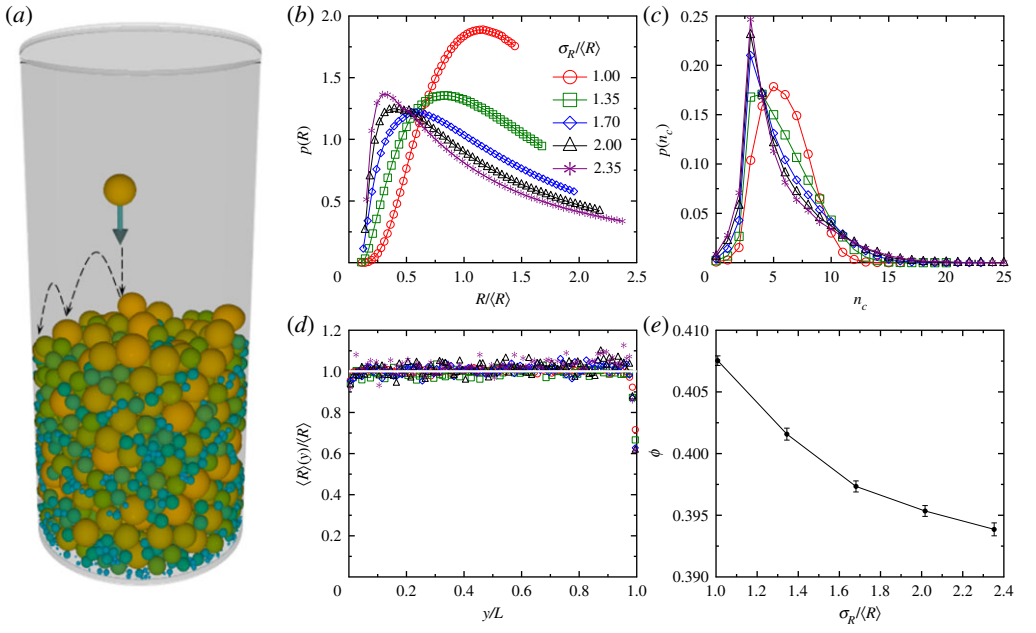

Figure 1. (*a*) Sample generation by sedimenting spherical particles in a cylindrical container. (*b*) Probability distribution of the radius of sedimenting spheres for the five different standard deviations σ_R considered. (*c*) Probability distribution of the number of contacts of the particles. (*d*) Average radius of the particles as a function of height along the cylinder axis. (*e*) Porosity of the sample as a function of the standard deviation σ_R of the radius. The legend for (*b–d*) is presented in (*b*).

samples in laboratory experiments [9,12]. The geometrical set-up and the sedimentation process is illustrated in figure 1*a*.

The radius of particles R was treated as a random variable sampled from a lognormal distribution, which is commonly found for the size of granules in reservoir rocks [9]. The sedimentation algorithm has the advantage that it is computationally efficient; however, it has the limitation that the range of particle size cannot be arbitrarily broad. Particles much smaller than the average can bounce through the voids of the sediment, creating a size segregation in the sample along the direction of gravity. On the contrary, voids around very large particles cannot be filled by smaller ones leading again to artefacts. Hence, we used the lognormal distribution

$$p(R) = \frac{1}{\sqrt{2\pi}s}\,\frac{1}{R}\exp\left(-(\ln R - \mu)^2/2s^2\right) \tag{2.1}$$

over a finite range $R_{\min} \le R \le R_{\max}$, where the ratio of the upper and lower bounds $R_{\max}/R_{\min}$ was carefully set [13]. In the density function equation (2.1), the parameters μ and s denote the mean and standard deviation of the logarithmized variable $\ln R$, respectively, or the geometric mean and geometric standard deviation in R. By contrast, the equivalent average (arithmetic mean) and standard deviation of the non-logarithmized sample values of the particle radius R will be denoted by $\langle R\rangle$ and σ_R in the following, respectively. In order to control the amount of micro-scale disorder in the materials' structure, samples were generated at different values of the standard deviation σ_R, while the average radius $\langle R\rangle$ was fixed. To characterize the degree of disorder in the sample, we use the dimensionless parameter $\sigma_R/\langle R\rangle$. Simulations were performed at five different values of $\sigma_R/\langle R\rangle = 1.0, 1.35, 1.7, 2.0, 2.35$, generating $K = 300$ samples with different realizations of disorder at each parameter set. To keep the average radius $\langle R\rangle$ fixed, the upper bound $R_{\max}$ was tuned to a constant value of the lower one $R_{\min}$ so that the ratio $R_{\max}/R_{\min}$ varied approximately between 12 and 20. The upper bound to this ratio was set by the requirement for random uniform packing of the spheres in the sedimentation process.

Greater standard deviations would have resulted in smaller particles settling preferentially at the bottom of the cylinder. While geologically realistic in some settings, our aim was to isolate spatially random, homogeneous, structural disorder as a control variable at this stage of the model development. Figure 1*b* shows the size distribution of particles $p(R)$ where the moving upper cut-off can also be observed. The total number of particles in a single cylinder fluctuates around 10^5.

Figure 1*c* demonstrates that the probability distribution $p(n_c)$ of the number of contacts n_c of the particles have an exponential tail, where for higher disorder the distributions cover a broader range with a slower decay. Only a small fraction of particles have a very low contact number $n_c < 3$. These are typically those particles which touch the container wall and have a low chance of establishing contact with other particles of the sample. In order to test the homogeneity of the sample, we determined the average radius of particles $\langle R\rangle(y)$ as a function of the position y measured along the cylinder axis, i.e. along the direction of gravity in the sedimentation process. Figure 1*d* shows that for each σ_R the value of $\langle R\rangle(y)$ fluctuates around the sample average $\langle R\rangle$, confirming that the specimen has a random uniform microstructure.

At higher disorder, particles fill the space more efficiently in the cylinder, so the porosity ϕ, i.e. the average fraction of voids in the numerical rock, decreases with increasing σ_R (figure 1*e*). However, while the degree of disorder $\sigma_R/\langle R\rangle$ is changed by more than a factor of 2, the porosity experiences only a small decrease of approximately 1%. In real rocks, there is a much bigger range of porosity which is caused by the significantly broader range of the particle size distribution associated with the greater complexity in the processes of sedimentation, re-working, cementation, pressure solution and induration not captured by our model at this stage [1,9,12].

3. Discrete element simulation of compressive failure

In order to form a porous digital rock, the random heterogeneous packing of particles generated by the sedimentation process must be completed with proper inter-particle interactions. For this purpose, we used our DEM, which has recently been introduced to investigate the compressive failure of heterogeneous materials [14,15]. In the model, cohesion between the particles is represented in such a way that the particles are coupled by beam elements along the edges of Delaunay triangles. The Delaunay triangulation is performed in three dimensions based on the centre-of-mass position of the particles in the initial configuration. It is a very important feature of the model that the physical properties of beams are determined by the initial packing: the length l_{ij} of the beam between particles i and j at positions $\boldsymbol{r}_i$ and $\boldsymbol{r}_j$ is obtained as the distance $l_{ij} = |\boldsymbol{r}_i - \boldsymbol{r}_j|$, while the beam's cross-sectional area A_{ij} is determined by the particles' radii R_i and R_j as $1/A_{ij} = 1/(R_i^2\pi) + 1/(R_j^2\pi)$. It follows that the randomness of the packing implies randomness of the spatial arrangement and physical properties of beam elements as well. Those particles which are not coupled by beams interact through Hertz contacts [16].

Under mechanical load, beams gradually deform and break according to a physical breaking rule when overstressed. The breaking criterion captures that failure is mainly caused by stretching and bending of beams

$$\left(\frac{\varepsilon_{ij}}{\varepsilon_{\mathrm{th}}}\right)^2 + \frac{\max(\varphi_i, \varphi_j)}{\varphi_{\mathrm{th}}} > 1. \tag{3.1}$$

Here, ε_{ij} denotes the axial strain of the beam between particles i and j, while φ_i and φ_j are the bending angles at the two beam ends. The breaking thresholds $\varepsilon_{\mathrm{th}}$ and φ_{th} remain constant, and control the relative importance of the stretching and bending modes of breaking [17]. The values of the two breaking parameters are fixed for all the beams, which implies that the structural disorder, introduced by the random particle packing is the only source of disorder in the model.

The equation of motion of the particles is solved numerically using a predictor–corrector scheme [18] to generate the time evolution of the system induced by external mechanical loading, including dynamic effects. The breaking criterion equation (3.1) is evaluated at each iteration step of the time evolution and those beams which fulfil the condition are removed, creating

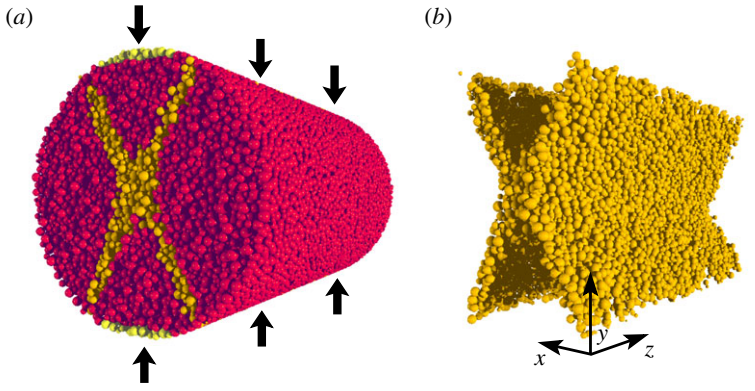

Figure 2. (*a*) Set-up of the Brazilian test. A cylindrical sample is compressed in a strain-controlled way. A few particle layers on the top and bottom of the sample are clamped, the top cap moves downward while the bottom is fixed. The two caps of the sample are highlighted by gold colour. (*b*) As a result, two damage bands emerge which cross each other in the middle of the sample. In (*a*), the sharply defined bands can be seen on the sample cross section also highlighted in yellow, while (*b*) presents only the damage bands spanning the entire sample. In (*b*), the axis of the (*x*, *y*, *z*) coordinate system of simulations is also illustrated. The origin of the coordinate system is in the middle of the base circle of the cylinder.

micro-cracks in the model. Further details of the model construction and the parameter settings can be found in [14,15]. The model has been tested under various loading conditions, including uniaxial tensile and compressive loading of bar [19] and cylindrical shaped specimens [14,15], and impact fragmentation of spherical bodies [19]. Detailed comparision of the evolving stress field, generated in spherical samples during impact against a hard wall, to corresponding finite-element calculations showed that the model captures all relevant components of the mechanics and fracture of heterogeneous brittle materials.

In the present study, a strain-controlled compression of cylindrical samples was simulated such that the compressive load was applied parallel to the diameter and perpendicular to the axis of the cylinder similar to the so-called Brazilian test, albeit with a greater ratio of length to diameter than typical for such a test in the laboratory for reasons outlined in §1 and in more detail in the text below [11]. In the simulations, a few particle layers of thickness $2R_{\max}$ on the top and bottom sides of the cylinder surface are clamped and the top layers are moved at a constant speed while the bottom ones are kept fixed (for illustration, see figure 2*a*). No confinement is imposed, so that outside the clamped regions surface particles are free to move. The simulation stops when the force acting on the top layer drops down to zero.

In our previous studies, the model was used to investigate the uniaxial compression of cylindrical samples focusing on both the time evolution of the fracture process [14,15,20] and on the spatial structure of the emerging damage [21]. We demonstrated that the gradual cracking proceeds in bursts of beam breakings, analogous to sources of acoustic emissions or crackling noise of real experiments. The model proved to be very successful in reproducing the observed power law statistics and exponents of burst sizes, energies, durations and waiting times between consecutive events [14,15,20]. The model also reproduced the observation in experiments that in the vicinity of failure localization occurs where micro-cracks concentrate in a narrow region resulting in the formation of a damage band [21]. Using finite size scaling arguments, we clarified that the damage band gets relatively sharper as the sample size increases [21].

Here, we focus on the effect of material disorder on the spatial structure of damage using a Brazilian-type loading set-up where cylindrical samples are slowly compressed diametrically perpendicular to the cylinder axis (figure 2). The system has the advantage that, due to geometrical constraints, extended damage bands are formed which span the sample parallel to the cylinder axis, and suffer less from edge effects in this direction than a standard experimental

Brazilian test on a shorter cylinder. This way good statistics can be achieved for the most important characteristic quantities of interest here. At each value of the disorder parameter $\sigma_R/\langle R\rangle$, the compression simulations were repeated $K = 300$ times to provide a statistical ensemble of models to account for uncertainties due to sample variability.

Computer simulations have revealed that the beginning of the fracture process is dominated by the structural disorder of the material which leads initially to spatially random crack nucleation. As the loaded system approaches failure, damage concentrates in two relatively narrow bands (figure 2). Owing to the geometrical constraints set by the clamped top and bottom caps of the sample, the two bands cross each other on the cylinder axis. Inside the damage band, the high concentration of micro-cracks results in the crushing of the material, creating a large number of small-sized fragments. To avoid the four large wedge-shaped fragments of largely intact rock, we identify the damage band as the set of those fragments which have a mass less than 20% of the total mass of the sample. In figure 2*a*, the damage bands are highlighted by colouring the particles according to the size of the fragment they belong to: fragments smaller than 20% of the sample size are yellow while the bigger ones comprising the four wedges are indicated by red colour.

4. Spatial position and structure of the damage band

The translational symmetry of the system along the direction of the cylinder axis implies that the damage band spans the entire sample with a rather uniform spatial structure along the cylinder axis. This is demonstrated by the side view of the damage band in figure 2*b* where the four wedges are omitted. The spatial uniformity is even more pronounced by the front views presented in figure 3, where the complete bands are presented for all disorders considered, but only the surface particles are visible since they shield those inside the sample.

The amount of disorder has a strong effect on the spatial position and structure of the damage band (figure 3). For low disorder, branches of the band are sharply defined in the sense that they comprise only a few particle layers bounded by a relatively smooth and straight surface. The band structure becomes systematically more diffuse as the amount of disorder increases, i.e. the branches gradually broaden, especially in the centre, and their connected core gets surrounded by a diffuse cloud of small-sized fragments.

Although the visual identification of the damage band in the sample is simple, the algorithmic determination of its precise position is rather complex in DEM simulations. To cope with the problem, recently we have developed a numerical procedure based on the spatial position of fragments inside the sample [21]. To adopt the method for the present geometry, we divided the x-shaped bands of figure 3 into four branches and analysed them separately. Using the cylindrical geometry, the centre-of-mass positions of all fragments of the damage bands are projected onto the x–y plane of the (x, y, z) coordinate system, i.e. the z coordinate of fragments is set to zero. (For the coordinate systems used, see figures 2*a* and 3*a*.) The straight lines were fitted to the point clouds in an iterative way using the least-squares method, gradually removing outliers which have the greatest deviation from the straight line. With a few iterations this method provides the position of the central line of the point cloud, which in turn identifies the central plane of the corresponding branch of the damage band (see figure 3*a* for illustration).

The position of the central plane of the band is characterized by the angle Θ it encloses with the load direction, i.e. with the vertical direction in figure 3. Owing to the structural disorder of the samples, the value of Θ fluctuates, so that it can be characterized by a probability distribution $p(\Theta)$. Simulations revealed that the values of the angle Θ obtained independently for the four branches of the damage band in a given sample are practically the same. Hence, each sample is characterized by a single value of Θ, the average of the four, and for each disorder parameter σ_R a unique distribution function $p(\Theta)$ is determined. Figure 4*a* shows that for all disorder values σ_R the distributions $p(\Theta)$ have a more-or-less symmetric form around an average $\langle\Theta\rangle$ which increases with σ_R. Figure 5 shows that the average orientation angle $\langle\Theta\rangle$ increases nearly linearly with $\sigma_R/\langle R\rangle$ while the error bars remain approximately the same. Rescaling the distributions $p(\Theta, \sigma_R)$ with the corresponding average $\langle\Theta\rangle$ and standard deviation σ_Θ of the orientation angle, the

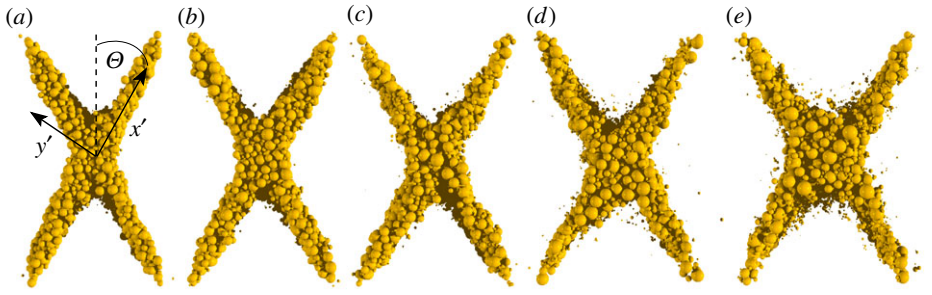

Figure 3. Front view of damage bands at different amounts of structural disorder σ_R. For the lowest disorder considered the band has sharp branches (*a*). Increasing disorder gives rise to broadening of the branches and the formation of a damage cloud surrounding the connected core of the band. In (*a*), the (x', y', z') coordinate system is highlighted which is used to determine the width of the band. The z' axis is perpendicular to the sample surface.

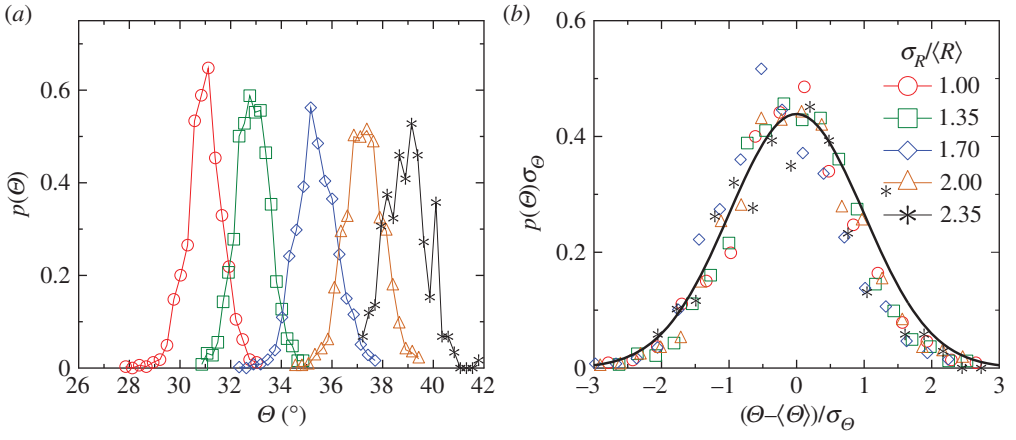

Figure 4. (*a*) Probability distribution $p(\Theta)$ of the angle Θ of the damage band with respect to the load direction for all the values of σ_R considered. The distributions always have the same functional form, but the average angle $\langle\Theta\rangle$ increases with the amount of disorder. Rescaling the distributions in (*b*) with the corresponding average $\langle\Theta\rangle$ and standard deviation σ_Θ, a good-quality collapse is obtained. The bold solid line represents the standard Gaussian. The two panels have the same legend presented in (*b*).

curves of different disorders σ_R can be convincingly collapsed on top of each other (figure 4*b*). The scaling function can be well approximated by the standard Gaussian, albeit with a small component of skew apparent in figure 4*b*.

In order to give a quantitative characterization of the internal structure of the damage band, we determined the probability distribution $p(y', \sigma_R/\langle R\rangle)$ of the y' coordinate of the centre of fragments measured from the central plane of the individual branches of the band. (For illustration of the (x', y', z') coordinate system, see figure 3*a*). Calculations showed that for each value of σ_R the four branches of the damage band have the same structure; hence, the band is characterized by a single distribution as the combination of the individual distributions of the four branches. We find that $p(y', \sigma_R/\langle R\rangle)$ has a bell-shaped functional form symmetric around the origin $y' = 0$ (see figure 6*a*). This confirms that the estimated central plane of the band is accurate. It follows that the thickness of the damage band W can be quantified by the width of the distributions $p(y', \sigma_R/\langle R\rangle)$ which monotonically increases with σ_R. The result is consistent with the direct observation of the bands in figure 3 where the broadening of the band occurs with increasing disorder.

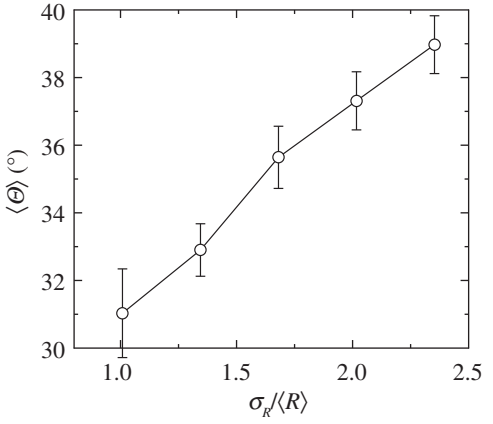

Figure 5. Average orientation angle $\langle \Theta \rangle$ of the central plane of the damage band as a function of the amount of disorder σ_R together with error bars.

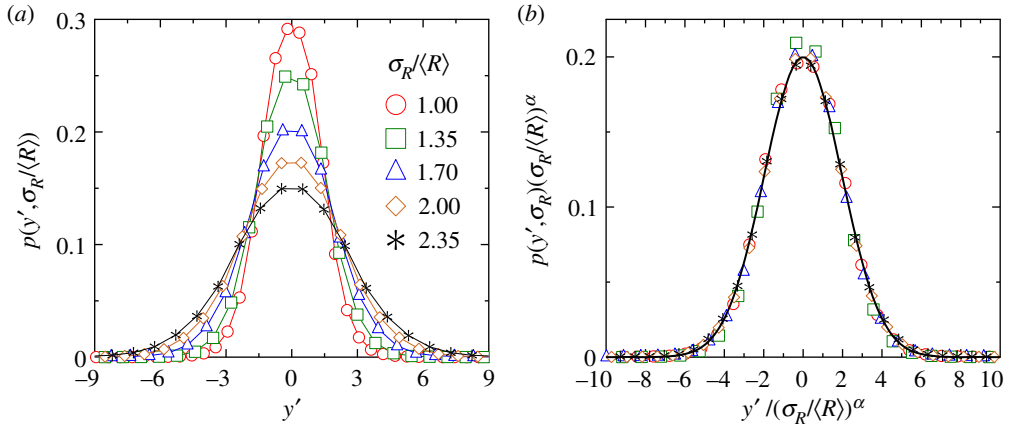

Figure 6. Probability distribution of the coordinate y' of fragments measured from the central plane of the damage band (*a*). The thickness of the band can be quantified by the width of the distributions which increases with the amount of meso-scale disorder σ_R. Rescaling the distributions with an appropriate power α of $\sigma_R/\langle R \rangle$, the distributions can be collapsed on top of each other (*b*). The continuous line represents a fitted Gaussian according to equation (4.3).

Figure 6*b* demonstrates the rescaling of the $p(y', \sigma_R/\langle R \rangle)$ curves with a proper power α of $\sigma_R/\langle R \rangle$, whence the distributions obtained at different amounts of disorder collapse on top of each other. Owing to the normalization of the distributions, the same value of the exponent α has to be used along both axes for the rescaling transformation.

The high-quality data collapse validates the scaling structure

$$p(y', \sigma_R/\langle R \rangle) = (\sigma_R/\langle R \rangle)^{\alpha} \Psi(y'/(\sigma_R/\langle R \rangle)^{\alpha}), \tag{4.1}$$

where $\Psi(x)$ denotes the scaling function. It also follows that the width W of the damage band has a power law dependence on the amount of disorder

$$W \sim (\sigma_R/\langle R \rangle)^{\alpha}. \tag{4.2}$$

Best collapse was achieved in figure 6*b* with a universal exponent $\alpha = 0.78 \pm 0.03$ so that W increases sub-linearly with the amount of disorder. The scaling function can be very well

described by a Gaussian functional form

$$\Psi(x) \sim \frac{1}{\sqrt{2\pi}\sigma_G} e^{-x^2/2\sigma_G^2}, \tag{4.3}$$

which is represented by the continuous line in figure 6*b*. The excellent agreement of the scaling function with the standard Gaussian was obtained tuning only the multiplication factor in equation (4.3), since $\Psi(x)$ is not normalized.

5. Fragmentation

Inside the damage band, the high concentration of micro-cracks gives rise to fragmentation of the porous material. As a representative example, figure 7 highlights the fragments of a sample of the highest disorder $\sigma_R/\langle R\rangle = 2.35$ considered. Most of the fragments are single particles, which represent the fine powder in the model. The high powder fraction indicates that by the time the sample falls apart the material has become greatly crushed. Larger fragments comprising a number of particles are embedded inside the powder. The frequency of fragments rapidly decreases with their size. The size of fragments is limited by the band width so that the cut-off fragment mass is much smaller than the sample size.

The statistics of fragments is characterized by the mass distribution of pieces which is shown in figure 8 for all values of σ_R considered. The emergence of damage bands sets strong constraints on the form of the size distribution. Outside the damage band, four large fragment wedges are formed between the branches of the band. As loading proceeds, these large fragments may break up into two or three smaller ones, but still remain much larger than the debris pieces inside the band. Consequently, a hump is formed on the mass distribution in the regime $m \approx m_0$ highlighted by the grey area in figure 8. Here m_0 denotes the average total mass of the samples. The mass distribution of fine powder of single particles is determined by the initial disorder of the system so that the $p(m)$ curves strongly differ in the small mass regime as σ_R is varied. The most remarkable feature of the fragment statistics is that, for intermediate size debris pieces of the damage band, comprising more than two particles, the distributions can be well approximated by a power law functional form

$$p(m) \sim m^{-\tau}, \tag{5.1}$$

followed by a short cut-off regime. Between the cut-off mass and the hump associated with large pieces (shaded grey in figure 8), a broad gap is formed without any fragment since the size of the fragments is limited by the size of the damage band. Figure 8 shows that the mass distribution exponent τ is universal, i.e. it does not depend on the amount of disorder, and the curves of different σ_R practically fall on the top of each other. The value of the exponent τ was determined by fitting $\tau = 2.4 \pm 0.06$. However, the total number of fragments and the cut-off mass of the power law regime both depend on the degree of disorder.

Since the fragments are confined to a relatively narrow band inside the cylindrical specimen, it can be expected that their shape exhibits anisotropy. To quantify the shape anisotropy, we determined the average mass of fragments $\langle m\rangle$ as a function of their radius of gyration R_g, where R_g is defined as

$$R_g^2 = \frac{1}{n}\sum_i^n (\boldsymbol{r}_i - \boldsymbol{r}_c)^2. \tag{5.2}$$

Here r_c denotes the centre-of-mass position of the fragment and the sum runs over its particles of number n. Figure 9 shows that the $\langle m\rangle(R_g)$ curves have a power law functional form

$$\langle m\rangle \sim R_g^D \tag{5.3}$$

as expected; however, they exhibit a crossover between two power law regimes of different exponents. For small fragment masses the value of the exponent D coincides with the dimension of the embedding space $D = 3 \pm 0.05$. At a certain fragment mass m_c, crossover occurs to a lower exponent $D = 2.65 \pm 0.05$. The two exponents are independent of the degree of disorder, but the

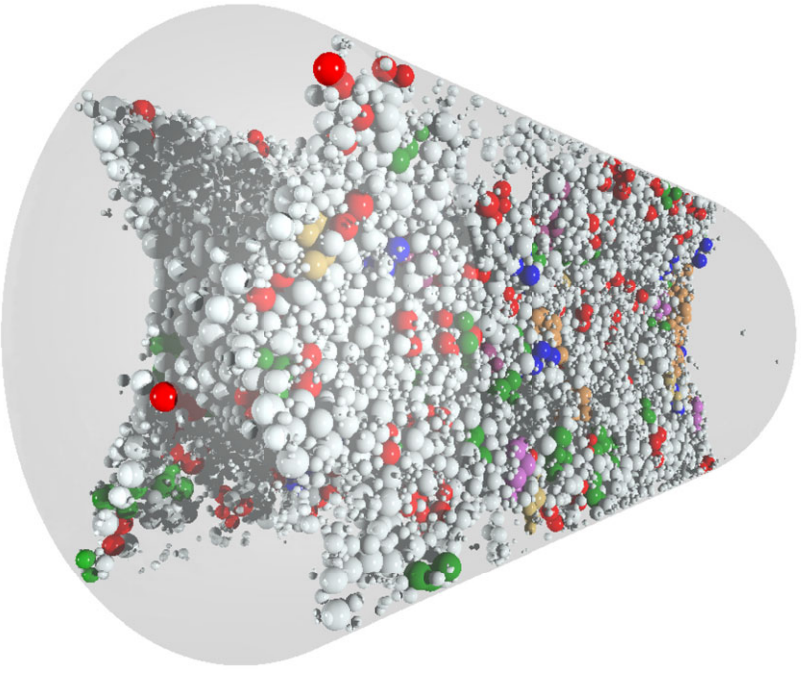

Figure 7. Fragments inside the damage band of a sample of the highest disorder $\sigma_R/\langle R\rangle = 2.35$ considered. Particles are coloured according to the size of the fragment they belong to: *grey*, *red*, *green*, *blue*, *purple*, *light brown* and *dark brown* colours stand for fragments comprising one, two, three, four, five and more than five particles, respectively. The four largest fragments, which fill the extended volumes bounded by the branches of the damage band, are skipped.

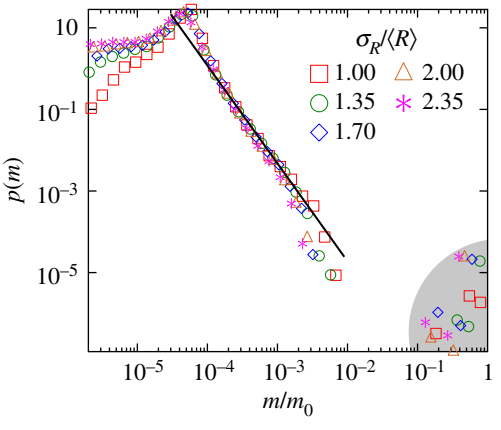

Figure 8. Mass distribution of fragments for all the disorder amplitudes σ_R. The hump of large fragments is highlighted by the grey area.

crossover mass m_c and size R_g^c depend on σ_R (figure 9*a*). This finding is remarkable because the fragments are essentially space-filling objects without any other sign of fractality. Recently, we have shown analytically that the exponent value lower than the embedding dimension $D < d$ is the consequence of the self-affine behaviour of fragment shapes, i.e. due to the geometrical constraints set by the narrow band, fragments are elongated and they become relatively flatter

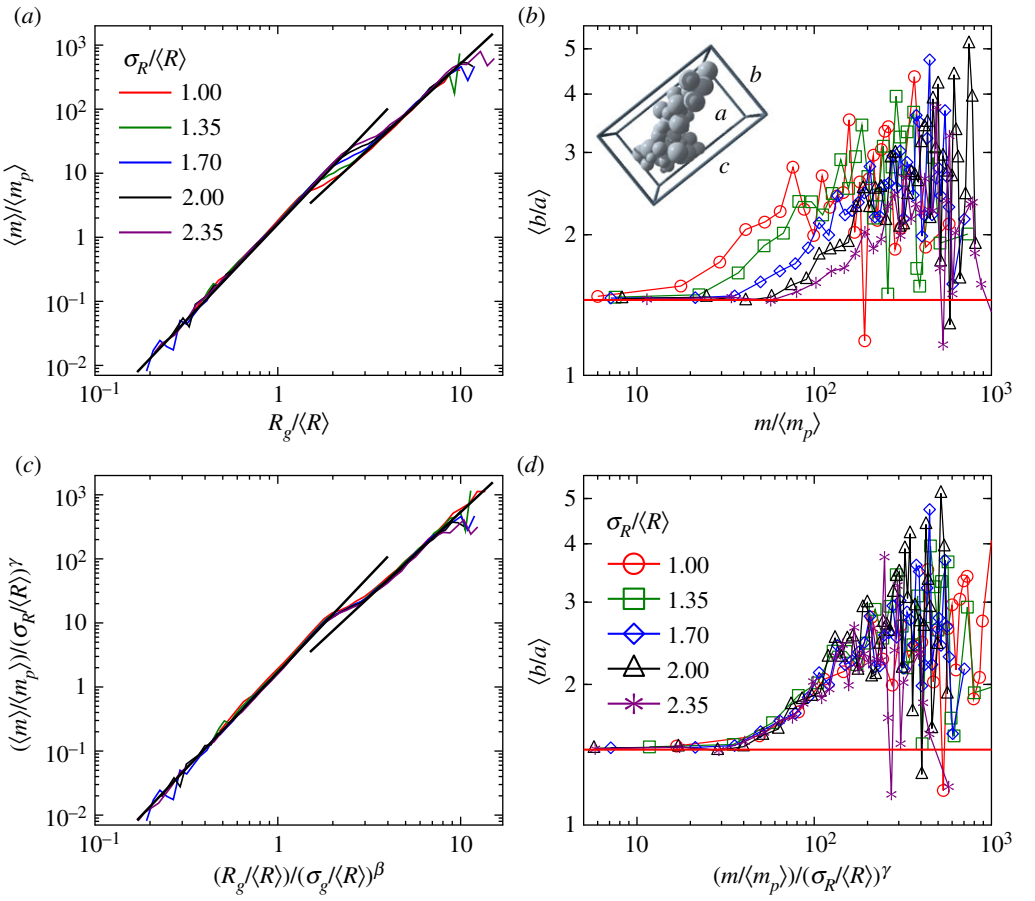

Figure 9. (*a*) Average mass of fragments $\langle m\rangle$ as a function of their radius of gyration R_g. A crossover is obtained between two power law regimes with different exponents. The two straight lines represent the fitted power law curves. (*b*) Average value of the ratio of the two sides $\langle b/a\rangle$ of the bounding box of fragments as a function of their mass m. Panels (*c*,*d*) present the same data as (*a*) and (*b*) just rescaled with powers of the degree of disorder.

with increasing maximum length [21–23]. The value of the exponent D obtained for $R_g > R_g^c$ falls very close to the fractal dimension $D = 2.6 \pm 0.11$ of natural fault damage zones [24].

In order to have a more direct measure of fragment shapes, we determined the bounding box of all the pieces inside the damage band. To capture the geometrical constraint of the band, bounding boxes were constructed in such a way that one side of the band is fixed to be parallel, while another one perpendicular, to the central plane of the band. For illustration see the inset of figure 9*b*. The bounding box has three different side lengths $a < b < c$, where the smallest one a is typically the one perpendicular to the damage band, while the other two b and c are parallel to the band's central plane. The anisotropy of the shape of pieces can be characterized, for example, by the ratio b/a which takes values greater than 1. Figure 9*b* shows that for small fragments the average shape parameter $\langle b/a\rangle$ takes a constant value close to one, $\langle b/a\rangle \approx 1.45$. Deviations start at a characteristic mass m_c where the increase of $\langle b/a\rangle$ sets in, indicating the increasing anisotropy for larger fragments. Note that for higher disorder, where the damage band is broader, the crossover starts at higher fragment masses.

A very interesting outcome of the data analysis is that shape descriptors $\langle m\rangle(R)$ and $\langle b/a\rangle(m)$ of fragments exhibit scaling with respect to disorder. Rescaling both R_g and $\langle m\rangle$ in figure 9*c* with appropriate powers β and γ of σ_R, curves of different amount of disorder can be collapsed on top

of each other. Best collapse is achieved with the exponents $\beta = 0.65$ and $\gamma = 2.0$ for R_g and $\langle m \rangle$, respectively. The consistency of the results is further supported by the scaling collapse presented in figure 9*d* which was achieved using the same value of the γ exponent along the horizontal axis. The results imply that the crossover mass m_c, which separates isotropic and anisotropic fragment shapes, scales as

$$m_c \sim (\sigma_R / \langle R \rangle)^{\gamma}. \tag{5.4}$$

Since for the corresponding crossover size R_g^c the relation $m_c \sim (R_g^c)^3$ holds, the two exponents β and γ are not independent, $\gamma = 3\beta$. Substituting the numerical values, the relation of the two exponents is verified to a good precision. We note that the characteristic fragment size R_g^c should be proportional to the width of the damage band $R_g^c \sim W$, which implies the relation $\alpha = \beta$ of the scaling exponents. This scaling relation is only approximately fulfilled by our numerical values.

6. Discussion and conclusion

Compressive failure of heterogeneous materials is governed by the spontaneous emergence of damage bands where the high concentration of micro-cracks leads to fragmentation. Based on a DEM of porous rocks, we presented a detailed study of the effect of the degree of meso-scale disorder on the overall position and internal structure of damage bands. Strain-controlled compression of cylindrical samples was simulated in a Brazilian-type test geometry which was modified to ensure the emergence of two conjugate damage bands with a sufficiently large along-axis extension.

We showed that the orientation angle the damage bands enclose with the load direction fluctuates around an average value, which increases linearly with the amount of disorder while its standard deviation remains approximately the same. The increasing orientation angle implies a decrease of the coefficient of internal friction of the material with increasing disorder.

The degree of disorder proved to have a strong effect on the structure of the damage band: at low disorder the bands are sharply defined with smooth surfaces; however, increasing disorder leads to gradual broadening which is accompanied by the formation of a diffuse cloud of damage around the bands' connected core. By means of data collapse analysis of the spatial distribution of fragments around the central plane of the damage band, we showed that the band width increases as a power law of the disorder amplitude with the exponent $\alpha = 0.78$.

Inside the damage band the material undergoes fragmentation, creating a large number of pieces with a broad variation of sizes. The majority of fragments form a powder phase comprising only single particles which embed larger pieces. Between the branches of the damage band four fragment wedges are formed which are significantly larger than the debris pieces inside the damage band. In the intermediate range, the mass distribution of fragments proved to be a power law with a universal exponent. The universality of the fragment statistics can be attributed to the robust mechanism of self-similar sequential break-up [25] where only the number of fragments and the cut-off size can be affected by the amount of disorder. The value of the exponent $\tau = 2.4$ is somewhat larger than the one found in uniaxial compression of cylindrical samples [21]; however, it still compares well with experimental findings on geomaterials [1].

To characterize the overall shape and structure of individual debris pieces, we showed that the average mass of fragments increases as a power law of their radius of gyration. However, at a characteristic fragment size a crossover occurs from the exponent $D = 3$ of space-filling compact objects to a lower one $D = 2.65$, which falls close to the fractal dimension of natural fault damage zones [24]. We demonstrated that this crossover is caused by the confined geometry of the damage band which sets constraints on the shape of fragments. Small fragments proved to have an isotropic shape; however, beyond a characteristic size, crossover occurs to an anisotropic flat shape. The crossover size was found to increase as a power law of the degree of disorder, being practically proportional to the width of the damage band.

An important outcome of our study is that, although global characteristics of the material's structure such as the porosity hardly changed when the disorder amplitude was varied, the

spatial structure of the emerging damage suffered relevant quantitative changes. The result shows that details of the damage process are sensitive to the strength of disorder; however, this effect can be cast into scaling laws in terms of the disorder amplitude. Our results have important implications for understanding the structure of damage zones from the scale of laboratory experiments to geological faults.

To promote shear failure and the formation of well-defined damage bands, in our study the external load was applied on a clamped surface area of the cylinder, which had a fixed extension about one-fourth of the sample diameter. It is a very interesting question how the results change when gradually shrinking the loaded area to approach the loading conditions of the standard Brazilian test. Since local failure gets more and more dominated by tensile stresses, a structural transition is expected from the conjugate shear bands to a single damage zone along the load direction where splitting of the specimen occurs. Work on this problem is in progress. A partly similar problem has recently been addressed in [26] where the breaking of cylindrical shaped particles was studied by varying the geometrical configuration of three loading plates. Peculiar damage patterns were obtained when moving away from the standard Brazilian test geometry.

Data accessibility. This article has no additional data.

Authors' contributions. I.V. generated the numerical rock samples. F.K. carried out computer simulations. G.P. and F.K. performed the data analysis. I.G.M. and F.K. conceived of and designed the study, and drafted the manuscript. All authors read and approved the manuscript.

Competing interests. The author(s) declare that they have no competing interests.

Funding. The work is supported by the EFOP-3.6.1-16-2016-00022 project. The project is co-financed by the European Union and the European Social Fund. This research was supported by the National Research, Development and Innovation Fund of Hungary, financed under the K-16 funding scheme Project No. K 119967. The research was financed by the Higher Education Institutional Excellence Programme of the Ministry of Human Capacities in Hungary, within the framework of the Energetics thematic programme of the University of Debrecen.

References

1. Turcotte DL. 1997 *Fractals and chaos in geology and geophysics*. Cambridge, UK: Cambridge University Press.
2. Turcotte DL. 1986 Fractals and fragmentation. *J. Geophys. Res.* **91**, 1921. (doi:10.1029/JB091iB02p01921)
3. Main I. 1996 Statistical physics, seismogenesis, and seismic hazard. *Rev. Geophys.* **34**, 433–462. (doi:10.1029/96RG02808)
4. Aström JA. 2006 Statistical models of brittle fragmentation. *Adv. Phys.* **55**, 247–278. (doi:10.1080/00018730600731907)
5. Morrow CA, Byerlee JD. 1989 Friction phenomena in rock experimental studies of compaction and dilatancy during frictional sliding on faults containing gouge. *J. Struct. Geol.* **11**, 815–825. (doi:10.1016/0191-8141(89)90100-4)
6. Ramos O, Cortet PP, Ciliberto S, Vanel L. 2013 Experimental study of the effect of disorder on subcritical crack growth dynamics. *Phys. Rev. Lett.* **110**, 165506. (doi:10.1103/PhysRevLett.110.165506)
7. Vasseur J, Wadsworth FB, Lavallée Y, Bell AF, Main IG, Dingwell DB. 2015 Heterogeneity: the key to failure forecasting. *Sci. Rep.* **5**, 13259. (doi:10.1038/srep13259)
8. Hawkes I, Mellor M. 1970 Uniaxial testing in rock mechanics laboratories. *Eng. Geol.* **4**, 179–285. (doi:10.1016/0013-7952(70)90034-7)
9. Mair K, Main I, Elphick S. 2000 Sequential growth of deformation bands in the laboratory. *J. Struct. Geol.* **22**, 25–42. (doi:10.1016/S0191-8141(99)00124-8)
10. Main IG, Kwon O, Ngwenya BT, Elphick SC. 2000 Fault sealing during deformation-band growth in porous sandstone. *Geology* **28**, 1131–1134. (doi:10.1130/0091-7613(2000)28<1131:FSDDGI>2.0.CO;2)
11. Li D, Wong LNY. 2013 The Brazilian disc test for rock mechanics applications: review and new insights. *Rock Mech. Rock Eng.* **46**, 269–287. (doi:10.1007/s00603-012-0257-7)

12. Sammonds PR, Meredith PG, Main IG. 1992 Role of pore fluids in the generation of seismic precursors to shear fracture. *Nature* **359**, 228–230. (doi:10.1038/359228a0)
13. Oakes R. 1991 The log-log-normal distribution. MS thesis, University of South Carolina, Columbia, SC, USA.
14. Kun F, Varga I, Lennartz-Sassinek S, Main IG. 2013 Approach to failure in porous granular materials under compression. *Phys. Rev. E* **88**, 062207. (doi:10.1103/PhysRevE.88.062207)
15. Kun F, Varga I, Lennartz-Sassinek S, Main IG. 2014 Rupture cascades in a discrete element model of a porous sedimentary rock. *Phys. Rev. Lett.* **112**, 065501. (doi:10.1103/PhysRevLett.112.065501)
16. Pöschel T, Schwager T. 2005 *Computational granular dynamics*. Berlin, Germany: Springer.
17. Timár G, Kun F, Carmona HA, Herrmann HJ. 2012 Scaling laws for impact fragmentation of spherical solids. *Phys. Rev. E* **86**, 016113. (doi:10.1103/PhysRevE.86.016113)
18. Allen MP, Tildesley DJ. 2002 *Computer simulation of liquids*. Oxford, UK: Clarendon Press.
19. Carmona HA, Wittel FK, Kun F, Herrmann HJ. 2008 Fragmentation processes in impact of spheres. *Phys. Rev. E* **77**, 051302. (doi:10.1103/PhysRevE.77.051302)
20. Pál G, Raischel F, Lennartz-Sassinek S, Kun F, Main IG. 2016 Record-breaking events during the compressive failure of porous materials. *Phys. Rev. E* **93**, 033006. (doi:10.1103/PhysRevE.93.033006)
21. Pál G, Jánosi Z, Kun F, Main IG. 2016 Fragmentation and shear band formation by slow compression of brittle porous media. *Phys. Rev. E* **94**, 053003. (doi:10.1103/PhysRevE.94.053003)
22. Domokos G, Kun F, Sipos AA, Szabó T. 2015 Universality of fragment shapes. *Sci. Rep.* **5**, 9147. (doi:10.1038/srep09147)
23. Kun F, Wittel FK, Herrmann HJ, Kröplin BH, Maloy KJ. 2006 Scaling behaviour of fragment shapes. *Phys. Rev. Lett.* **96**, 025504. (doi:10.1103/PhysRevLett.96.025504)
24. Sammis CG, Biegel RL. 1989 Fractals, fault-gouge, and friction. *Pure Appl. Geophys.* **131**, 255–271. (doi:10.1007/BF00874490)
25. Wittel FK, Kun F, Herrmann HJ, Kröplin BH. 2004 Fragmentation of shells. *Phys. Rev. Lett.* **93**, 035504. (doi:10.1103/PhysRevLett.93.035504)
26. Neveu A, Artoni R, Descantes Y, Richard P. 2017 Effect of contact anisotropy on the crushing strength of aggregates. *EPJ Web Conf.* **140**, 07010. (doi:10.1051/epjconf/201714007010)